

PCCP

Accepted Manuscript



This is an *Accepted Manuscript*, which has been through the Royal Society of Chemistry peer review process and has been accepted for publication.

Accepted Manuscripts are published online shortly after acceptance, before technical editing, formatting and proof reading. Using this free service, authors can make their results available to the community, in citable form, before we publish the edited article. We will replace this *Accepted Manuscript* with the edited and formatted *Advance Article* as soon as it is available.

You can find more information about *Accepted Manuscripts* in the [Information for Authors](#).

Please note that technical editing may introduce minor changes to the text and/or graphics, which may alter content. The journal's standard [Terms & Conditions](#) and the [Ethical guidelines](#) still apply. In no event shall the Royal Society of Chemistry be held responsible for any errors or omissions in this *Accepted Manuscript* or any consequences arising from the use of any information it contains.

Bi-temple assisted synthesis of mesoporous manganese oxide nanostructures: Tailoring properties for efficient CO oxidation

Mouni Roy, Somjyoti Basak, and Milan Kanti Naskar*

Sol-Gel Division, CSIR-Central Glass and Ceramic Research Institute, Kolkata 700 032, India

ABSTRACT: A simple soft bi-templating process was employed for the synthesis of mesoporous manganese oxides nanostructures using KMnO_4 as precursor, polyethylene glycol (PEG) and cetyltrimethylammonium bromide (CTAB) as templates in the presence of benzaldehyde as organic additive under alkaline medium, followed by calcinations at $400\text{ }^\circ\text{C}$. XRD and Raman spectroscopic analysis of the calcined products confirmed the existence of stoichiometric (MnO_2 and Mn_5O_8) and non-stoichiometric mix phase ($\text{MnO}_2 + \text{Mn}_5\text{O}_8$) of Mn oxides obtained by tuning additive concentration and synthesis time. The surface properties of the prepared Mn oxides were determined by XPS analysis. Mesoporosity of the samples was confirmed by N_2 adsorption-desorption study. Variation of synthesis condition resulted in the formation of different morphologies i.e., nanoparticles, nanorods and nanowires of the Mn oxides ($\alpha\text{-MnO}_2$, Mn_5O_8 , and $\alpha\text{-MnO}_2 + \text{Mn}_5\text{O}_8$). The synthesized mesoporous Mn oxide nanostructures were applied for the catalytic oxidation of harmful air pollutant, carbon monoxide (CO). Mn_5O_8 nanoparticles having highest BET surface area, and non-stoichiometric manganese oxide ($\alpha\text{-MnO}_2 + \text{Mn}_5\text{O}_8$) nanorods with higher Mn^{3+} concentration rendered better catalytic efficiency.

*Corresponding author. E-mail: milan@cgcri.res.in, Fax: +91 33 24730957

1. INTRODUCTION:

Manganese oxides are important class of inexpensive, non-toxic and environmentally benign materials for their potential applications in the fields of catalysis, toxic waste remediation, and battery technology.^{1,2} Porous manganese oxides are of special research interest as heterogeneous catalyst for ozone decomposition,³ photocatalytic oxidation of organic pollutants,⁴ nitric oxide reduction,⁵ selective oxidations of carbon monoxide,⁶ volatile organic compounds (VOC) ⁷ and hydrogen peroxide decomposition⁸ etc., because of their large surface area, nanosized walls, and variable oxidation states.⁹ Manganese oxides are generally prepared by normal thermal treatment,¹⁰ hydrothermal ¹¹⁻¹³ sol gel,¹⁴ reflux ^{15,16} etc. methods. During the past few years, researchers reported for the synthesis of manganese oxides of different morphologies like sphere, rod, sheet, tube, cube, flower-like etc.¹⁷⁻²¹

Manganese oxides crystallizes with different oxidation states of manganese (Mn^{2+} , Mn^{3+} and Mn^{4+}) to form tunnel and/or layered structures.²² The layered 2D structures possess infinite, edge shared MnO_6 octahedra with interlayer species, which can easily be modified to different manganese oxide phases.^{23,24} Small cations as charge neutralizers furnished by permanganate precursors reside inside the tunnel structure of manganese oxides for the coexistence of their different oxidation states. It is reported that the layered structure of manganese oxides obtained by sol-gel method is transformed to high crystalline different tunnel structures under hydrothermal and/or post-synthetic thermal treatment.²⁵ However, synthesis of high crystalline mesoporous manganese oxides with tunable oxidation states is becoming challenging because of growth of nanocrystals during high temperature annealing process. There are few reports on solution based process in which the as-prepared products are annealed to render stable stoichiometric and/or non-stoichiometric manganese oxides.²⁶⁻²⁹ Birnessite-type single oxidation state layered structures of Mn oxides are widely studied.

However, there are few literature reports on the formation of binary metastable layered Mn_5O_8 having compositional formula $\text{Mn}_2^{2+} \text{Mn}_3^{4+}\text{O}_8$.³⁰⁻³² A schematic representation of the crystal structure of (A) layered monoclinic Mn_5O_8 and (B) $\alpha\text{-MnO}_2$ having K^+ ions incorporated in its tunnel structure is shown in Fig. 1.

Metastable layered Mn_5O_8 phase is obtained by different techniques, like heating of Mn_3O_4 at 250-550°C under nitrogen-oxygen atmosphere, heating of MnO under oxygen flow, decomposition of $\beta\text{-MnOOH}$ in air, decomposition of $\gamma\text{-MnOOH}$ in nitrogen atmosphere etc.^{26,33} KMnO_4 as low cost and easily available Mn source is commonly used to synthesize different forms of Mn oxides. Most of the researchers used acidic³⁴⁻³⁸ or neutral³⁹⁻⁴¹ medium for reduction of higher oxidation states of Mn (in permanganate) to its lower oxidation states. However, reduction of KMnO_4 in alkaline medium⁴² is very rare. Ching et. al.⁴³ synthesized MnO_2 using carboxylic acid as an additive. With the motivation of the above literature survey, we conceived that benzaldehyde could play a significant role as reducing additive for the formation of different Mn oxides (non-stoichiometric and stoichiometric) under alkaline medium.

In the present study, mesoporous nanostructured Mn oxides (non-stoichiometric and stoichiometric) were prepared using KMnO_4 and aqueous based cationic (CTAB) and non-ionic (PEG 600) bi-templates in the presence of benzaldehyde as reducing additive under alkaline condition, followed by thermal treatment. In this investigation, the synthesis time (2-20 h) and additive concentration (20-80 mmol) were tuned to obtain stoichiometric (with pure phase Mn_5O_8 and $\alpha\text{-MnO}_2$) and non-stoichiometric (a mix phase of $\text{Mn}_5\text{O}_8 + \alpha\text{-MnO}_2$) Mn oxides. The crystal structure, textural property, microstructure analysis and surface property of the products were performed.

Catalytic oxidation of CO is important in many practical applications, such as air purification, pollution control devices, CO removal in heavy industry, CO gas sensors, purification of hydrogen for proton-exchange fuel cells etc.⁴⁴ There are different types of oxidation catalysts which transform CO into CO₂. For oxidation catalysis, the precious metals like Au, Pd, Ru, Pt, Ir and Rh are generally used. However, keeping in mind the cost factor, considerable efforts have been made to searching transition metal oxides for catalytic oxidation of CO. For catalytic oxidation of ethyl acetate (a VOC) Cu, Co, Fe, La, Ni oxides have been used.⁴⁵ Carabineiro *et al.*⁴⁶ studied the catalytic oxidation of CO using CeO₂ and Au/CeO₂. Catalytic properties for CO oxidation have been reported by many researchers.⁴⁷⁻⁵¹ With this motivation, in the present study the catalytic oxidation of carbon monoxide (CO) with the synthesized products of Mn oxides was illustrated.

To the best of our knowledge it is the first time we report a soft bi-templating synthesis approach in the presence of benzaldehyde as reducing additive under alkaline condition for the synthesis of different stoichiometric and non-stoichiometric Mn oxides nanostructures as efficient, cost-effective catalyst for CO oxidation.

2. EXPERIMENTAL SECTION

2.1. Materials: All the chemicals were of analytical grade, and used without any further purification. Anhydrous KMnO₄, polyethylene glycol 600 (PEG 600) and benzaldehyde were received from Merck while cetyltrimethylammonium bromide (CTAB) was obtained from Sigma Aldrich. Deionized water (DI) water was used throughout the experiment.

2.2. Synthesis of mesoporous nanostructured Mn oxides: In a typical synthesis process, 8 mmol of CTAB solution was added into 70 ml aqueous solution of PEG 600 (5 wt. %) under stirring. The pH of the solution was adjusted to 8 by slow addition of 1M KOH. 10 mmol

KMnO₄ was added into the above mix solution followed by addition of 40 mmol benzaldehyde. The whole mixture was stirred for 2h to obtain a black product. It was then collected by centrifugation, washed with DI water, and dried at 60°C for 4h. The dried samples were calcined at 400°C for 2h to obtain highly crystalline Mn oxides mesoporous nanostructures. The above reaction was performed by changing the concentration of benzaldehyde to 20 and 80 mmol keeping the reaction time 2h, and also by changing the reaction time for 10 and 20h keeping the concentration of benzaldehyde at 40 mmol. The samples were designated as S-2@20, S-2@40 and S-2@80 for benzaldehyde concentration of 20, 40 and 80 mmol, respectively, with 2h reaction time, while those were marked as S-10@40 and S-20@40 for reaction time of 10 and 20h, respectively with a fixed benzaldehyde concentration of 40 mmol.

2.3. Characterizations: X-ray diffraction (XRD) studies were performed by a Philips X'Pert Pro XRD (Model: PW 3050/60) with Ni-filtered Cu-K_α radiation ($\lambda = 0.15418$ nm), operating at 40 kV and 30 mA. The thermal behaviors of the uncalcined particles were studied by thermogravimetry (TG) and differential thermal analysis (DTA) with Netzsch STA 449C, Germany from room temperature to 600 °C in air atmosphere at the heating rate of 5 °C/min. The Raman spectra were recorded using a RENISHAW spectrometer with 514 nm radiation from an Ar laser at room temperature. X-ray photoelectron spectroscopy (XPS) measurements were carried out in a PHI 5000 Versaprobe II Scanning XPS microprobe (ULVAC-PHI, USA). The spectra were recorded with monochromatic AlK_α ($h\nu = 1486.6$ eV) radiation with an overall energy resolution of ~0.7 eV. The morphology of the particles was examined by field emission scanning electron microscopy (FESEM) (Model: Zeiss, SupraTM 35VP, Oberkochen, Germany) operating with an accelerating voltage of 10 kV, and transmission electron microscopy (TEM), using a Tecnai G2 30ST (FEI) instrument operating at 300 kV. Nitrogen adsorption-desorption measurements were conducted at 77 K

with a Quantachrome (ASIQ MP) instrument. The powders were outgassed in vacuum at 200°C for 4 h prior to the measurement. The surface area was determined by Brunauer-Emmett-Teller (BET) method within the relative pressure (p/p_0) range of 0.05-0.20 and the pore size distributions were calculated by the Barrett-Joyner-Halenda (BJH) method. The total pore volume was estimated from the amount of nitrogen adsorbed at the relative pressure (p/p_0) of ca 0.99.

2.4. Catalytic test: The experimental set-up for catalytic test is schematically shown in Fig. S1, ESI. The catalytic test for CO oxidation was performed in a continuous flow fixed-bed glass tubular reactor (internal diameter = 4 mm). In a typical catalytic test, 50 mg of catalyst (Mn-oxides) were used in each experiment. Before catalytic test, the catalyst was pre-treated with a mix gas comprising of 80 vol% He and 20 vol% O₂ with a flow rate of 40 mLmin⁻¹ for 30 min. After pre-treatment, a standard reaction gas mixture containing 1 vol% CO, 20 vol% O₂ and balance with N₂ was passed through the catalyst bed at a flow rate of 40 mLmin⁻¹. The weigh hourly space velocity (WHSV) was 48000 mLg⁻¹h⁻¹. The conversion of CO was measured by on-line gas chromatography (Varian CP3800) equipped with a thermal conductivity detector (TCD) after the catalyst bed temperature was stabilized for 30 min to obtain a steady state. The area under the peak was used to calculate the % CO conversion. Percentage of CO conversion was calculated using the following equation:

$$\% \text{ conversion} = \text{Area under CO}_2 \text{ peak} / (\text{Area under CO peak} + \text{Area under CO}_2 \text{ peak}) \dots\dots(1)$$

The conversion of CO to CO₂ was measured at different temperatures. The conversion rate of CO per unit surface area per unit second was obtained from the following equation.

$$\text{Conversion rate [mol.s}^{-1}\text{m}^{-2}] = C_{\text{CO}} * (X_{\text{CO}}/100) / (0.05 * \text{SA}) \dots\dots(2)$$

Where, C_{CO} is the number of moles of CO passed through the catalyst per second, X_{CO} denotes the percent CO conversion and the factor $[0.05 * \text{SA}]$ represents a specific surface area

for 50 mg of catalyst (Mn oxides). The calculated rates are normalized to the surface area of Mn oxides.

3. RESULTS AND DISCUSSION

3.1. Characterization of synthesized Mn oxide samples: Figure 2 shows the XRD patterns of the synthesized Mn oxide samples: (a) S-2@20, (b) S-2@80, (c) S-2@40, (d) S-10@40 and (e) S-20@40. Monoclinic Mn_5O_8 phase (JCPDS file no. 39-1218) was appeared for the samples prepared with (a) 20 and (c) 40 mol of benzaldehyde for 2h reaction time each. Interestingly, the samples (b) prepared with 80 mmol benzaldehyde for 2h reaction time and (d) prepared with 40 mmol benzaldehyde with 10h reaction time exhibited a mix phase of monoclinic Mn_5O_8 and tetragonal $\alpha\text{-MnO}_2$ (JCPDS file no. 44-0141), the latter phase is shown in the insets of Fig. 2(b) and (d), respectively. It is to be noted that a non-stoichiometric composition of Mn oxides was obtained in the presence of higher concentration of benzaldehyde (80 mmol) with shorter reaction time (2h), and also medium concentration of benzaldehyde (40 mmol) with medium reaction time (10h). However, the sample (e) prepared with 40 mmol benzaldehyde for 20h reaction time revealed pure tetragonal $\alpha\text{-MnO}_2$ phase. It is worth noting that by changing the concentrations of benzaldehyde, and also the reaction time, different phases (stoichiometric and non-stoichiometric) of Mn oxides were obtained. DTA and TGA of the uncalcined samples are shown in Fig. S2 (ESI): (A) S-2@20, (B) S-2@80, (C) S-2@40, (D) S-10@40 and (E) S-20@40. In TG analysis, it is observed that the mass loss occurred in two distinct steps, i.e., up to around 170°C and 170-300°C. The curves show the broad endothermic peaks below 150°C in the DTA curves, accompanied a mass loss of about 5-8% which was attributed to the removal of adsorbed water. A significant amount of mass loss (around 40-50%) was noticed for the temperature range of 170-300°C. In the DTA curves, two exothermic peaks at

around 220-240°C and 270-290°C could be attributed to the decomposition of residual organic templates (CTAB and PEG)⁵²⁻⁵⁴ and additives (benzaldehyde) present in the samples. However, the endothermic peaks at around 260-270°C was assigned to the removal of structural water and hydroxides ions.

Raman spectra of the synthesized samples: (a) S-2@20, (b) S-2@80, (c) S-2@40, (d) S-10@40 and (e) S-20@40 are shown in Fig. 3. For the samples prepared with (a) 20 mmol of benzaldehyde for 2h reaction time, the Raman bands at 261, 300, 428, 474, 532, 575, 620 and 649 cm^{-1} represent Raman active modes of Mn_5O_8 belonging to $C2/m$ space group with $7A_g+4B_g$ Raman active modes in which the band at 649 cm^{-1} was most intense A_g mode. It confirmed the presence of phase pure monoclinic Mn_5O_8 nanoparticles in the sample.⁵⁵ However, for the sample prepared with (c) 40 mmol of benzaldehyde for 2h reaction time, a little shifting of the above Raman bands occurred toward lower wavenumber. It could be due to size effect of Mn_5O_8 nanowires. It is reported that anisotropic growth of Mn_5O_8 nanorods rendered Raman bands shift by 1-3 cm^{-1} .⁵⁶ Interestingly, for the sample (e) prepared with 40 mmol benzaldehyde for 20h reaction time, the Raman bands at 326, 387, 504, 570 and 634 cm^{-1} signify the formation of tetragonal $\alpha\text{-MnO}_2$ with K^+ ion (denoted as K-MnO_2) incorporated inside its tunnel structure.⁵⁷ It is mentioned worthy that from XRD analysis it becomes difficult to distinguish tetragonal $\alpha\text{-MnO}_2$ phase with and without encapsulation of K^+ ion inside the tunnel structure. However, the Raman study is more sensitive to crystalline disorders as well as local structural properties⁵⁸ to identify whether K^+ ion is encapsulated in the tunnel structure of $\alpha\text{-MnO}_2$ or not. Structurally $\alpha\text{-MnO}_2$ crystallizes in bcc tetragonal phase with space group $I4/m$ indicating $6A_g+6B_g+3E_g$ Raman active modes. But all of the above predicted modes were not observed. The bands at ~ 574 and ~ 634 cm^{-1} represent A_g spectroscopic species that originate from breathing vibrations of MnO_6 octahedra present

within tetragonal framework. It is emphasized that the relative intensities of the above two high frequency bands were concurrent to the nature of tunnel species.⁵⁹ It is to be noted that during precipitation of MnO_2 , K^+ ions of the precursors were adsorbed followed by their encapsulation into the tunnel structure of MnO_2 after calcinations. It may be illustrated that α - MnO_2 is a hollandite type material consisting of (2×2) and (1×1) tunnel structures. A variety of stabilizing cations, such as Na^+ , Li^+ , H_3O^+ , NH_4^+ , K^+ , Pb^{2+} and Ba^{2+} ions furnished by the precursors during synthesis are situated in the large (2×2) tunnels, whereas the small (1×1) tunnels remains empty.^{60,61} For the sample S-2@80, the characteristic Raman bands at 265, 300, 428, 476, 537, 578, 620 and 650 cm^{-1} , and those at 269, 302, 428, 475, 645 cm^{-1} for the sample S-10@40 signify the presence of Mn_5O_8 phase. Interestingly, the existence of K-MnO_2 in both the samples, S-2@80 and S-10@40 was also confirmed by the appearance of bands at 510 and 632 cm^{-1} , and 332, 388, 510, 575 and 754 cm^{-1} , respectively.

For the analysis of surface elemental composition, determination of exact oxidation state of the metal in the oxides, and the concentration of lattice oxygen and surface oxygen defect, XPS study of Mn oxides was performed. Figure 4 illustrates the (A) $\text{Mn}2\text{p}_{3/2}$, (B) $\text{O}1\text{s}$, and (C) $\text{Mn}3\text{s}$ XPS spectra of the different Mn oxides: (a) S-2@20, (b) S-2@80, (c) S-2@40, (d) S-10@40 and (e) S-20@40. It was observed that the $\text{Mn}2\text{p}_{3/2}$ peak could be decomposed into three component peaks at binding energies (BE) *ca.* 640.2, 641.4 and 642.8 eV which were attributed to Mn^{2+} , Mn^{3+} and Mn^{4+} species,^{27, 62, 63} respectively, present in different Mn oxides (stoichiometric and non-stoichiometric). Quantitative analysis of Mn^{n+} ($n = 2-4$) content, molar ratios of $\text{Mn}^{3+}/\text{Mn}^{4+}$ and $\text{Mn}^{3+}/\text{Mn}^{2+}$ obtained from the $\text{Mn}2\text{p}_{3/2}$ spectra of all the samples was summarized in Table 1. From the above results, it is obvious that for stoichiometric composition of Mn_5O_8 (S-2@20, S-2@40) and non-stoichiometric composition of $(\text{Mn}_5\text{O}_8 + \text{MnO}_2)$ (S-2@80, S-10@40), Mn^{2+} , Mn^{3+} and Mn^{4+} coexist.

Interestingly, for stoichiometric composition of Mn_5O_8 , Mn^{3+} is reduced significantly to Mn^{2+} with increase in benzaldehyde concentration from 20 to 40 mmol, while for non-stoichiometric composition of $(\text{Mn}_5\text{O}_8 + \text{MnO}_2)$, more reduction to Mn^{2+} occurred with 80 mmol benzaldehyde concentration. It signifies that benzaldehyde played a significant role for the reduction of Mn^{3+} ions to Mn^{2+} ions. For stoichiometric composition of MnO_2 , maximum amount of Mn^{4+} ions is observed in the presence of Mn^{3+} ions. The asymmetrical signal of O1s spectra of Mn oxide samples (Fig. 4B) show the binding energies of 529.4, 531.0 and 532.8 eV, which were assigned to lattice oxygen (O_α), surface oxygen defect (O_β) and adsorbed OH^- group and/or molecular water,^{64,65} respectively. The corresponding concentrations of O_α , O_β and surface adsorbed OH^- / molecular water were evaluated (Table 1). It is noticed that the sample S-20@40 having higher concentration of Mn^{4+} , and that of S-2@40 with higher concentration of Mn^{2+} , render maximum amount of O_β and O_α species, respectively. Tang *et al.*²⁷ reported that higher oxidation state of Mn oxide (Mn^{4+}) generates more O_β species, whereas its lower oxidation state (Mn^{2+}) produce oxygen vacancy promoting the mobility of lattice oxygen (O_α species). From Mn3s spectra (Fig. 4C), the average oxidation state (AOS) of Mn oxides was calculated using the relationship $\text{AOS} = 8.956 - 1.126(\Delta E_s)$.⁶⁶ Table S1, ESI summarizes the ΔE_s and AOS values of different Mn oxides, where ΔE_s represents Mn3s multiplet splitting i.e., binding energy obtained from doublet separation of Mn3s. A significant decrease in ΔE_s , and increase in AOS values could be due to the presence of pure α - MnO_2 phase obtained from the sample S-20@40.⁵⁹ Thus, from AOS values it was confirmed that more oxidized Mn species were present in the sample S-20@40 compared to other samples having lower AOS values.

Figure 5 depicts FESEM images of Mn oxide samples: a) S-2@20, (b) S-2@80, (c) S-2@40, (d) S-10@40 and (e) S-20@40, (the corresponding higher magnified images are indicated in Figs. 5f-j). It is observed that for lower concentration of benzaldehyde (20 mmol)

with 2h reaction time (Fig. 5a,f), the agglomerated nanoparticles (50-100 nm) were obtained. For higher concentration of benzaldehyde (80 mmol) with 2h reaction time, nanorod (50-150 nm) particles assembled together containing some agglomerated nanoparticles (Fig. 5b,g). Interestingly with medium concentration of benzaldehyde (40 mmol), nanowires like particles were self-assembled to nest-like morphology (Fig. 5c, h). For a fixed concentration of benzaldehyde (40 mmol), the nanowire particles obtained for 2h reaction time were converted to nanorod-like particles with increase in reaction time to 10h (Fig. 5d,i) and 20 h (Fig. 5e,j).

Figure 6 shows TEM images of Mn oxide samples: a) S-2@20, (b) S-2@80, (c) S-2@40, (d) S-10@40 and (e) S-20@40, (the corresponding higher magnified images (Figs. 6f-j) are indicated with circle mark). Aggregation of smaller nanocrystals was revealed for lower concentration of benzaldehyde (20 mmol) with shorter reaction time (Fig. 6a, f), while higher concentration of benzaldehyde (80 mmol) with shorter reaction time rendered nanorod assembly in the presence of aggregated nanoparticles (Fig. 6b,g). However, nanowire-like particles obtained with 40 mmol benzaldehyde for 2h reaction time (Fig. 6c, h) was transformed to nanorod-like particles with increase in reaction time to 10h (Fig. 6d, i) and 20h (Fig. 6e,j). The energy dispersive X-ray spectroscopy (EDS) of the samples (inset of Fig. 6f-j) indicates the presence of Mn and O in different ratios (the C and Cu atoms appeared from the grid). It is worth noting that K atom was present in the samples S-2@80, S-10@40 and S-20@40, indicating the formation of K-MnO₂ phase which was supported by Raman study. The HR-TEM images of the samples (Figs. 6k,m,o,q,s for S-2@20, S-2@80, S-2@40, S-10@40 and S-20@40, respectively) revealed the respective lattice fringes of Mn₅O₈ and α -MnO₂ of different Mn oxides. For the samples S-2@20 and S-2@40, the lattice fringes of 0.49 and 0.495 nm corresponded to the (200) and (-110) crystal planes, respectively of Mn₅O₈. However, the sample S-2@80 show the lattice fringes of 0.49 and 0.284 nm

corresponding to the lattice planes of (200) and (-310) of α -MnO₂/Mn₅O₈ and Mn₅O₈, respectively; the sample S-10@40 indicates the lattice fringe of 0.69 nm corroborated to the lattice plane of (110) of α -MnO₂. The presence of phase pure α -MnO₂ in the sample S-20@40 was confirmed by the lattice fringe of 0.49 nm assigned to (200) crystal planes. The above results were supported by XRD and Raman analysis. The SAED pattern of the sample S-2@20 (Fig. 6l) show the concentric rings of bright diffraction spots signifying the polycrystalline nature of the particles. Interestingly, the SAED pattern of nanowire (S-2@40, Fig. 6p) and nanorod (S-2@80 (Fig. 6m), S-10@40 (Fig. 6r) and S-20@40 (Fig. 6t)) like particles revealed linearly arranged bright electron diffraction spots indicating the single crystalline nature of the particles. In these cases smaller primary nanoparticles fuse together and orient in a fashion to form nanorod like particles following ‘oriented attachment’ growth mechanism.⁶⁷

Fig. 7A shows the nitrogen adsorption–desorption isotherms of different Mn oxides: a) S-2@20, (b) S-2@80, (c) S-2@40, (d) S-10@40 and (e) S-20@40. All the isotherms display type IV plots according to IUPAC classification indicating mesoporous characteristics of the sample. The H-3 type hysteresis loops in the isotherms indicated existence of asymmetric, interconnected, slit-like mesoporosity in the samples.⁶⁸ The BJH pore size distributions (PSDs) of the corresponding samples derived from desorption data of the isotherms are shown in the Fig. 6B. The sample S-2@20 exhibited wider pore size distribution compared to the other samples. The textural properties of Mn oxides are shown in Table S2 (ESI). For a shorter reaction time of 2h, BET surface area, pore volume and pore diameter decreased significantly with increase in benzaldehyde concentration from 20 mmol to 80 mmol. In this case benzaldehyde could reduce the templating effect of PEG and CTAB rendering reduction in surface area and pore volume of Mn oxides. Interestingly, with increase in reaction time from 2h to 10h at a fixed concentration (40 mmol) of benzaldehyde, surface area and pore

volume decreased followed by increase in the same values with increasing reaction time from 10h to 20h. The phase transformation of mix phase $\text{Mn}_5\text{O}_8 + \text{MnO}_2$ to $\alpha\text{-MnO}_2$ phase from the sample S-10@40 to S-20@40 could be the reason for such sudden change.

A probable formation mechanism for the synthesis of Mn oxides is illustrated in Fig. 8. In aqueous medium CTAB forms micelle. The self-assembly of the micelles takes place with the association of polar “head” groups pointing towards outer surface with aqueous part and a nonpolar “oil core” (consisting of nonpolar “tail” groups) remaining away from the aqueous solution. The PEG molecules stabilized the CTAB micelles through wrapping around the micellar aggregates.⁶⁹ In the presence of KMnO_4 , MnO_4^- ions surrounding the micelles interact with the cetyltrimethylammonium cations (CTA^+) of CTAB and PEG molecules *via* electrostatic and/or hydrogen bonding interaction. Under alkaline condition, MnO_4^- is reduced to MnO_2 ,⁷⁰ in which K^+ ions are trapped as is evidenced by Raman study. It is worth mentioning that benzaldehyde played a significant role in tuning the morphology and phase transformation of Mn oxides. To establish the effect of benzaldehyde, a blank experiment was performed for 2h (Experimental section 2.2) in the absence of benzaldehyde (The sample ID is S-2@0). To investigate the crystal structures of the prepared sample (S-2@0), XRD (Figure S3(A), ESI†) and Raman spectra (Figure S3(B), ESI†) were recorded. The results revealed the formation of K^+ ion trapped in tetragonal $\alpha\text{-MnO}_2$ phase instead of formation of monoclinic Mn_5O_8 which was obtained for the sample S-2@40 (prepared with benzaldehyde). Thus the above experimental data confirmed that benzaldehyde has a significant role in tuning the crystallographic phase of Mn oxides.

Moreover, it is interesting to note that organic species present in organic-inorganic hybrid materials play a significant role in the formation of well developed nanostructures via supramolecular arrangement of intercalated organic moieties.⁷¹ In the present study the

morphology (FESEM image) of S-2@0 sample (prepared without benzaldehyde) was found to be agglomerated particle of Mn oxides (Figure S4, ESI†) instead of formation of Mn oxide nanowires which was obtained for the sample S-2@40 (prepared with benzaldehyde). It is worth mentioning that benzaldehyde (organic species) not only influences the crystallographic phase, it also shows certain impact on the morphology of the resulting Mn-oxides (inorganic species). Many research groups investigated that organic species like benzaldehyde⁷² and/or in-situ generated benzyl benzoate species⁷³ (produced upon condensation of the products obtained by Cannizzaro-like reaction of benzaldehyde in alkaline medium) assisted controlled anisotropic growth of the formed nanoparticles. Djerdj *et al.*⁷⁴ showed that in-situ formed benzoate molecule binds to the specific crystal face of lanthanum hydroxide which directs 1D growth of nanoparticles. In the present study an optimum benzaldehyde concentration of 40 mmol was required for the synthesis of 1D structure (Fig. 5c,h) of Mn oxides. However, 20 mmol benzaldehyde with the same reaction time exhibited Mn oxide nanoparticles (Fig. 5a,f). On increasing the concentration of benzaldehyde to 80 mmol (Fig. 5b,g) the 1D structures were assembled via co-operative growth and assembly process.⁷¹ Interestingly, with increase in reaction time to 10-20h for 40 mmol benzaldehyde, the self assembled 1D structure (nanorod-like) of Mn oxides were also noticed. Generally, the surface adsorbed phenyl rings attain special “T-shaped” orientation with respect to each other such that they undergo “edge-to-face” van der Waal interactions. This attractive interaction lowers the surface energy and provides stability to the resulting assembled nanorod structure.

3.2 Catalytic performance: The synthesized Mn oxides show catalytic activity for the oxidation of toxic air pollutant carbon monoxide (CO). Fig 9 shows the (A) percentage (%) conversion of CO with temperature, (B) bar chart of different % of CO oxidation i.e., 10%, 50%, 90% and 100% corresponding to their respective temperatures i.e., T₁₀, T₅₀, T₉₀ and T₁₀₀,

and (C) The Arrhenius plots [\ln (conversion rate) vs. $1/T$] for CO oxidation, in presence of different Mn oxides: a) S-2@20, (b) S-2@80, (c) S-2@40, (d) S-10@40 and (e) S-20@40. The temperatures corresponding to different % of CO oxidations are shown in Table S3 (ESI). It is clear that the trend in catalytic efficiency for CO oxidation followed in the order of S-2@20 > S-10@40 > S-2@80 > S-20@40 > S-2@40 (Fig. 9A,B and Table S3). The maximum catalytic performance of S-2@40 was due to its enhanced surface area, pore volume and pore diameter.^{75,76} To compare the catalytic activity for CO oxidation with different catalyst having different surface area, the calculated rates were normalized on the surface area of the catalyst. The activation energy (E_a) was calculated from the slope of the linear plot (Fig. 9C). Lower is the E_a , more active is the catalyst toward CO oxidation. Based on the activation energy, S-10@40 having lowest E_a (17.0 kJ/mole) showed higher catalytic efficiency, while the sample S-2@40 with highest E_a (77.1 kJ/mole) rendered lowest catalytic activity. Comparing with other literature data (Table S4, ESI), the product S-10@40 showed lowest E_a exhibiting highest catalytic efficiency for CO oxidation. Even at low temperature (at 100°C) the catalytic activity of Mn-oxides obtained by bi-templated method was found to be comparable with that of same materials synthesized by Carabineiro *et. al.*⁷⁷ The catalytic activity can be explained on the bonding nature of $Mn^{n+}-CO$ species. It is noteworthy that catalytic efficiency depends on adsorption of CO molecule on the catalytic surface (Mn^{n+}) followed by desorption as CO_2 molecules by weakening of $Mn^{n+}-CO$ bond. According to molecular orbital (MO) theory, the σ electrons - highest occupied molecular orbital (HOMO) of CO molecule interact with vacant d orbital of Mn^{n+} forming $Mn^{n+} \leftarrow CO$ (σ -HOMO) bonding, while the filled d orbital electrons of metal (Mn^{n+}) interact with vacant $2\pi^*$ - lowest unoccupied molecular orbital (LUMO) of CO molecule forming $Mn^{n+} \rightarrow CO$ ($2\pi^*$ - LUMO) π -back bonding. The adsorption of CO on catalytic surface is favoured with weaker $Mn^{n+} \leftarrow$

CO (σ -HOMO) and $\text{Mn}^{n+} \rightarrow \text{CO} \pi$ -back bonding favouring desorption (rate limiting step) of CO to CO_2 . It is obvious that for the lower oxidation of Mn (Mn^{2+}), $\text{Mn}^{2+} \rightarrow \text{CO} \pi$ -back bonding is stronger and $\text{Mn}^{2+} \leftarrow \text{CO} (\sigma\text{-HOMO})$ bonding is weaker, while for higher oxidation of Mn^{4+} , $\text{Mn}^{4+} \rightarrow \text{CO} \pi$ -back bonding is weaker and $\text{Mn}^{4+} \leftarrow \text{CO} (\sigma\text{-HOMO})$ bonding is stronger. Thus, Mn^{3+} could be more favourable to optimize bonding stability of $\text{Mn}^{3+}\text{-CO}$ toward CO oxidation. It is reported that due to stronger π -back bonding, $\text{Mn}^{2+}\text{-CO}$ species are more stable than $\text{Mn}^{3+}\text{-CO}$ species favouring lower activation energy of the latter species.⁷⁸ Therefore, the sample S-10@40 having higher Mn^{3+} content (from XPS results) could render higher catalytic efficiency whereas, the sample S-2@40 render lower catalytic efficiency due to the presence of higher Mn^{2+} content. Moreover, CO chemisorption is also dependent on the surface adsorbed $\text{OH}^-/\text{H}_2\text{O}$ concentration.¹⁷ This is because oxygen being much more electronegative than hydrogen; therefore, the electron density of O-H bond shifts toward oxygen, gaining partial positive charge by H atom. Thus, it interacts with 5σ electron containing CO molecule forming a stable adduct. From XPS data of O1s the $\text{OH}^-/\text{H}_2\text{O}$ concentration was determined (Table 1). The improved catalytic efficiency of S-10@40 was due to higher $\text{OH}^-/\text{H}_2\text{O}$ concentration.

From the above study, it is inferred that the catalytic activity of Mn oxides for CO oxidation is dependent on various factors like textural properties (surface area, pore volume and pore diameter), variation of oxidation states of metal ion, CO chemisorption determined by surface adsorbed $\text{OH}^-/\text{H}_2\text{O}$ concentration etc.

4. CONCLUSION:

In summary, we have synthesized mesoporous nanostructured Mn oxides with different crystalline phases *via* reduction of KMnO_4 under alkaline condition in the presence of benzaldehyde (as additive), using double templates (CTAB, PEG 600), followed by

calcination at 400°C. Different oxidation states of Mn oxides were confirmed by Raman and XPS studies. The morphology and textural properties of the particles were tuned by changing the benzaldehyde concentrations as well as reaction time. The catalytic activity of Mn oxides for the oxidation of CO, the highly environment pollutant was illustrated based on textural properties (surface area, pore volume and pore diameter), variation of oxidation states of metal ion, CO chemisorptions as determined by surface adsorbed OH⁻/H₂O concentration etc. The present method could be applicable for the synthesis of other transition metal oxides with tunable physico-chemical properties toward different catalytic applications.

Acknowledgement

The authors would like to thank the Director of this institute for his kind permission to publish this paper. M. Roy is thankful to CSIR for her fellowship. The Nano-structured Materials Division is thankfully acknowledged for Raman spectra. The work was funded by DST-SERB Project, Government of India (No. GAP 0616, Grant No.: SR/S3/ME/0035/2012),

References:

1. S. L. Suib, *J. Mater. Chem.*, 2008, **18**, 1623-1631.
2. Q. Feng, H. Kanoh and K. Ooi, *J. Mater. Chem.*, 1999, **9**, 319-333.
3. Y. Xi, C. Reed, Y.-K. Lee and S. T. Oyama, *J. Phys. Chem. B*, 2005, **109**, 17587-17596.
4. H. Cao and S. L. Suib, *J. Am. Chem. Soc.*, 1994, **116**, 5334-5342.
5. A. Patel, P. Shukla, J. Chen, T. E. Rufford, V. Rudolph and Z. Zhu, *Catal. Today*, 2013, **212**, 38-44.

6. J. Xu, Y.-Q. Deng, Y. Luo, W. Mao, X.-J. Yang and Y.-F. Han, *J. Catal.*, 2013, **300**, 225-234.
7. **S. S. T. Bastos, S. A. C. Carabineiro, J. J. M. Órfão, M. F. R. Pereira, J. J. Delgado and J. L. Figueiredo**, *Catal. Today*, 2012, **180**, 148-154.
8. S. C. Kim and W. G. Shim, *Appl. Catal., B*, 2010, **98**, 180-185.
9. M. Roy, S. Ghosh and M. K. Naskar, *Dalton Trans.*, 2014, **43**, 10248-10257.
10. Y. Muraoka, H. Chiba, T. Atou, M. Kikuchi, K. Hiraga, Y. Syono, S. Sugiyama, S. Yamamoto and J.-C. Grenier, *J. Solid State Chem.*, 1999, **144**, 136-142.
11. R. N. DeGuzman, Y.-F. Shen, E. J. Neth, S. L. Suib, C.-L. O'Young, S. Levine and J. M. Newsam, *Chem. Mater.*, 1994, **6**, 815-821.
12. X. Wang and Y. Li, *Chem. - Eur. J.*, 2003, **9**, 300-306.
13. G.-H. Qiu, H. Huang, S. Dharmarathna, E. Benbow, L. Stafford and S. L. Suib, *Chem. Mater.*, 2011, **23**, 3892-3901.
14. S. Ching, S. M. Hughes, T. P. Gray and E. J. Welch, *Microporous Mesoporous Mater.*, 2004, **76**, 41-49.
15. N. Kijima, H. Yasuda, T. Sato and Y. Yoshimura, *J. Solid State Chem.*, 2001, **159**, 94-102.
16. T. D. Xiao, P. R. Strutt, M. Benaissa, H. Chen and B. H. Kear, *Nanostruct. Mater.*, 1998, **10**, 1051-1061.
17. S. Liang, F. Teng, G. Bulgan, R. Zong and Y. Zhu, *J. Phys. Chem. C*, 2008, **112**, 5307-5315.
18. Y. Gao, Z. Wang, J. Wan, G. Zou and Y. Qian, *J. Cryst. Growth*, 2005, **279**, 415-419.
19. D. Zheng, S. Sun, W. Fan, H. Yu, C. Fan, G. Cao, Z. Yin and X. Song, *J. Phys. Chem. B*, 2005, **109**, 16439-16443.
20. C. Yuan, B. Gao, L. Su and X. Zhang, *J. Colloid Interface Sci.*, 2008, **322**, 545-550.

21. F. Wang, H. Dai, J. Deng, G. Bai, K. Ji and Y. Liu, *Environ. Sci. Technol.*, 2012, **46**, 4034-4041.
22. M. M. Thackeray, *Prog. Solid State Chem.*, 1997, **25**, 1-71.
23. M. Dolle, S. Patoux and M. M. Doeff, *Chem. Mater.*, 2005, **17**, 1036-1043.
24. Y. J. Park and M. M. Doeff, *Solid State Ionics*, 2006, **177**, 893-900.
25. X.-F. Shen, Y.-S. Ding, J. Liu, J. Cai, K. Laubernds, R. P. Zerger, A. Vasiliev, M. Aindow and S. L. Suib, *Adv. Mater. (Weinheim, Ger.)*, 2005, **17**, 805-809.
26. J. H. Lee, Y. J. Sa, T. K. Kim, H. R. Moon and S. H. Joo, *J. Mater. Chem. A*, 2014, **2**, 10435-10443.
27. W. Tang, X. Wu, D. Li, Z. Wang, G. Liu, H. Liu and Y. Chen, *J. Mater. Chem. A*, 2014, **2**, 2544-2554.
28. V. Iablokov, K. Frey, O. Geszti and N. Kruse, *Catal. Lett.*, 2010, **134**, 210-216.
29. K. Frey, V. Iablokov, G. Safran, J. Osan, I. Sajo, R. Szukiewicz, S. Chenakin and N. Kruse, *J. Catal.*, 2012, **287**, 30-36.
30. H. R. Oswald, W. Feitknecht and M. J. Wampetich, *Nature (London, U. K.)*, 1965, **207**, 72.
31. M. O. Michio Sugawara, Kenzo Matsuki, *Chem. Lett.*, 1991, **20**, 1465- 1468.
32. C. Klingsberg and R. Roy, *J. Am. Ceram. Soc.*, 1960, **43**, 620-626.
33. Z. Bai, B. Sun, N. Fan, Z. Ju, M. Li, L. Xu and Y. Qian, *Chem. - Eur. J.*, 2012, **18**, 5319-5324 .
34. S. Bag and C. Retna Raj, *J. Mater. Chem. A*, 2015, doi: 10.1039/C5TA08426A.
35. W. Xiao, D. Wang and X. W. Lou, *J. Phys. Chem. C*, 2010, **114**, 1694-1700.
36. Y. Wu, X. Yin, S. Xing, Z. Ma, Y. Gao and L. Feng, *Mater. Lett.*, 2013, **110**, 16-19.
37. Y. Liu, Z. Chen, C.-H. Shek, C. M. L. Wu and J. K. L. Lai, *ACS Appl. Mater. Interfaces*, 2014, **6**, 9776-9784.

38. Y. Tan, C. Xu, G. Chen, X. Fang, N. Zheng and Q. Xie, *Adv. Funct. Mater.*, 2012, **22**, 4584-4591.
39. L.-L. Yu, J.-J. Zhu and J.-T. Zhao, *Eur. J. Inorg. Chem.*, 2013, **2013**, 3719-3725.
40. P. K. Nayak and N. Munichandraiah, *Mater. Sci. Eng., B*, 2012, **177**, 849-854.
41. H. Chen, J. He, C. Zhang and H. He, *J. Phys. Chem. C*, 2007, **111**, 18033-18038.
42. L. Li, C. Nan, J. Lu, Q. Peng and Y. Li, *Chem. Commun. (Cambridge, U. K.)*, 2012, **48**, 6945-6947.
43. S. Ching, D. A. Kriz, K. M. Luthy, E. C. Njagi and S. L. Suib, *Chem. Commun. (Cambridge, U. K.)*, 2011, **47**, 8286-8288.
44. S. PalDey, S. Gedevanishvili, W. Zhang and F. Rasouli, *Appl. Catal. B*, 2005, **56**, 241-250.
45. X. Chen, S. A. C. Carabineiro, S. S. T. Bastos, P. B. Tavares, J. J. M. Órfão, M. F. R. Pereira and J. L. Figueiredo, *J. Environ. Chem. Eng.*, 2013, **1**, 795-804.
46. S. A. C. Carabineiro, S. S. T. Bastos, J. J. M. Órfão, M. F. R. Pereira, J. J. Delgado and J. L. Figueiredo, *Appl. Catal. A*, 2010, **381**, 150-160.
47. Z.-X. Li, F.-B. Shi, L.-L. Li, T. Zhang and C.-H. Yan, *Phys. Chem. Chem. Phys.*, 2011, **13**, 2488-2491.
48. K. Ramesh, L. Chen, F. Chen, Y. Liu, Z. Wang and Y.-F. Han, *Catal. Today*, 2008, **131**, 477-482.
49. W. Dingsheng, X. Run, W. Xun and L. Yadong, *Nanotechnology*, 2006, **17**, 979.
50. Y.-X. Miao, L.-H. Ren, L. Shi and W.-C. Li, *RSC Adv.*, 2015, **5**, 62732-62738.
51. T. Zaki and D. Aman, *Energy Sources, Part A*, 2012, **34**, 2147-2155.
52. V. Hariharan, S. Radhakrishnan, M. Parthibavarman, R. Dhilipkumar and C. Sekar, *Talanta*, 2011, **85**, 2166-2174.

53. S. C. Junggeburth, K. Schwinghammer, K. S. Viridi, C. Scheu and B. V. Lotsch, *Chem. - Eur. J.*, 2012, **18**, 2143-2152.
54. E. Karaoglu, H. Kavas, A. Baykal, M. S. Toprak and H. Sozeri, *Nano-Micro Lett.*, 2011, **3**, 79-85.
55. T. Gao, P. Norby, F. Krumeich, H. Okamoto, R. Nesper and H. Fjellvag, *J. Phys. Chem. C*, 2010, **114**, 922-928.
56. G. Gouadec and P. Colomban, *Progress in Crystal Growth and Characterization of Materials*, 2007, **53**, 1-56.
57. T. Gao, H. Fjellvag and P. Norby, *Anal. Chim. Acta*, 2009, **648**, 235-239.
58. Y. Li, J. Wang, Y. Zhang, M. N. Banis, J. Liu, D. Geng, R. Li and X. Sun, *J. Colloid Interface Sci.*, 2012, **369**, 123-128.
59. T. Gao, M. Glerup, F. Krumeich, R. Nesper, H. Fjellvag and P. Norby, *J. Phys. Chem. C*, 2008, **112**, 13134-13140.
60. J. E. Post, *Proc. Natl. Acad. Sci. U. S. A.*, 1999, **96**, 3447-3454.
61. Q. Feng, H. Kanoh, Y. Miyai and K. Ooi, *Chem. Mater.*, 1995, **7**, 148-153.
62. V. P. Santos, M. F. R. Pereira, J. J. M. Orfao and J. L. Figueiredo, *Appl. Catal., B*, 2010, **99**, 353-363.
63. Muilenberg G. E, 1979, (Minnesota: Perkin Elmer Corporation).
64. L. Yu, G. Diao, F. Ye, M. Sun, J. Zhou, Y. Li and Y. Liu, *Catal. Lett.*, 2011, **141**, 111-119.
65. K. Jiratova, J. Mikulova, J. Klempa, T. Grygar, Z. Bastl and F. Kovanda, *Appl. Catal., A*, 2009, **361**, 106-116.
66. V. R. Galakhov, M. Demeter, S. Bartkowski, M. Neumann, N. A. Ovechkina, E. Z. Kurmaev, N. I. Lobachevskaya, Y. M. Mukovskii, J. Mitchell and D. L. Ederer, *Phys. Rev. B: Condens. Matter Mater. Phys.*, 2002, **65**, 113102/113101-113102/113104.

67. R. L. Penn and J. F. Banfield, *Science (Washington, D. C.)*, 1998, **281**, 969-971.
68. M. Roy, S. Ghosh and M. K. Naskar, *Phys. Chem. Chem. Phys.*, 2015, **17**, 10160-10169.
69. P. Gianni, L. Bernazzani, R. Carosi and V. Mollica, *Langmuir*, 2007, **23**, 8752-8759.
70. S. Dash, S. Patel and B. K. Mishra, *Tetrahedron*, 2009, **65**, 707-739.
71. J. Polleux, N. Pinna, M. Antonietti and M. Niederberger, *J. Am. Chem. Soc.*, **2005**, **127**, 15595-15601.
72. J. Polleux, A. Gurlo, N. Barsan, U. Weimar, M. Antonietti and M. Niederberger, *Angew. Chem. Int. Ed.*, 2006, **45**, 261-265.
73. N. Pinna, G. Garnweitner, P. Beato, M. Niederberger and M. Antonietti, *Small*, **2005**, **1**, 112-121.
74. I. Djerdj, G. Garnweitner, D. Sheng Su and M. Niederberger, *J. Solid State Chem.*, 2007, **180**, 2154-2165.
75. N. Yi, Y. Cao, Y. Su, W.-L. Dai, H.-Y. He and K.-N. Fan, *J. Catal.*, 2005, **230**, 249-253.
76. N. Gunasekaran, S. Saddawi and J. J. Carberry, *J. Catal.*, 1996, **159**, 107-111.
77. S. A. C. Carabineiro, S. S. T. Bastos, J. J. M. Orfao, M. F. R. Pereira, J. J. Delgado and J. L. Figueiredo, *Catal. Lett.*, 2010, **134**, 217-227.
78. R. Craciun, B. Nentwick, K. Hadjiivanov and H. Knozinger, *Appl. Catal., A*, 2003, **243**, 67-79.

Figure Captions

Figure 1: Schematic representation of the crystal structure of (A) layered monoclinic Mn_5O_8 and (B) tetragonal $\alpha\text{-MnO}_2$ encapsulating K^+ ion inside its tunnel structure.

Figure 2: XRD patterns of Mn oxide samples: (a) S-2@20, (b) S-2@80, (c) S-2@40, (d) S-10@40 and (e) S-20@40, prepared at different reaction conditions.

Figure 3: Raman spectra of Mn oxide samples: (a) S-2@20, (b) S-2@80, (c) S-2@40, (d) S-10@40 and (e) S-20@40, prepared at different reaction conditions.

Figure 4: XPS spectra for (A) Mn $2p_{3/2}$, (B) O 1s, and (C) Mn 3s of Mn oxide samples (a) S-2@20, (b) S-2@80, (c) S-2@40, (d) S-10@40 and (e) S-20@40, prepared at different reaction conditions.

Figure 5: FESEM micrographs of Mn oxide samples (a) S-2@20, (b) S-2@80, (c) S-2@40, (d) S-10@40 and (e) S-20@40, (the corresponding higher magnified images are indicated in Figs. 5f-j)

Figure 6: (a-e) TEM images, (f-j) magnified TEM images (with EDS at the inset), (k,m,o,q,s) HRTEM, (l,n,p,r,t) SAED pattern of Mn oxide samples S-2@20 (a,f,k,l), S-2@80 (b,g,m,n), S-2@40 (c,h,o,p), S-10@40 (d,i,q,r) and S-20@40 (e,j,s,t), respectively.

Figure 7: (A) N_2 adsorption-desorption isotherms and (B) Pore size distributions of Mn oxide samples (a) S-2@20, (b) S-2@80, (c) S-2@40, (d) S-10@40 and (e) S-20@40, prepared at different reaction conditions.

Figure 8: Schematics of the proposed formation mechanism of Mn oxides.

Figure 9: (A) Percentage of CO conversion as a function of temperature, (B) Temperatures corresponding to 10 % (T_{10}), 50% (T_{50}), 90% (T_{90}) and 100 % (T_{100}) CO conversion, and (C) Arrhenius plot for CO oxidation with Mn oxide catalyst: (a) S-2@20, (b) S-2@80, (c) S-2@40, (d) S-10@40 and (e) S-20@40.

Figures

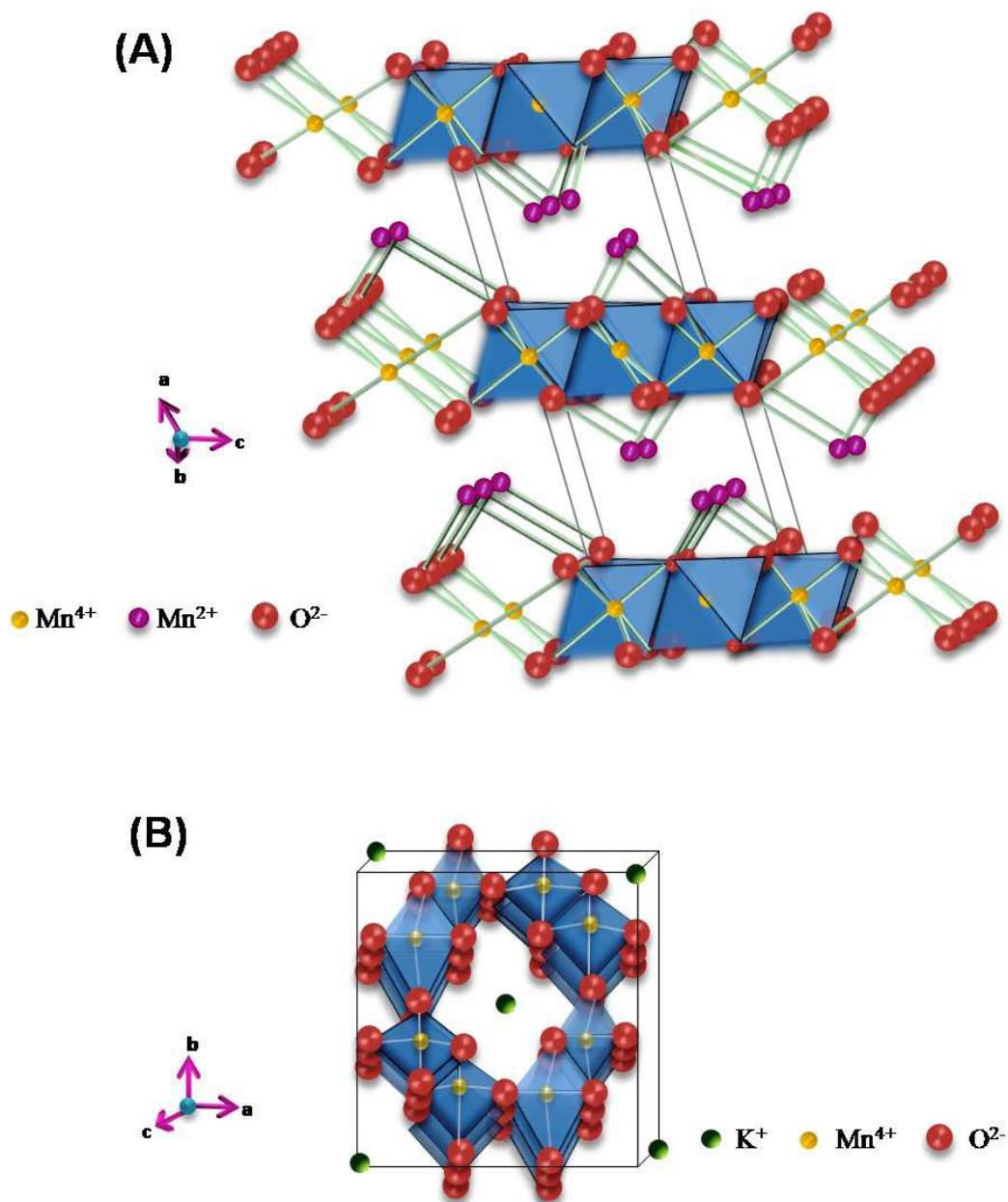


Figure 1: Schematic representation of the crystal structure of (A) layered monoclinic Mn_5O_8 and (B) tetragonal $\alpha\text{-MnO}_2$ encapsulating K^+ ion inside its tunnel structure.

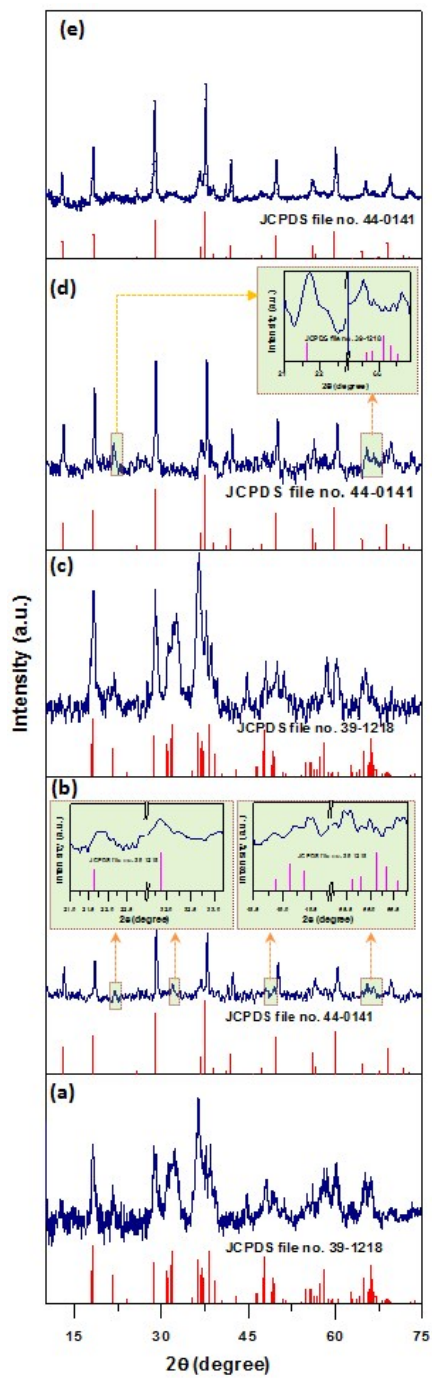


Figure 2: XRD patterns of Mn oxides samples: (a) S-2@20, (b) S-2@80, (c) S-2@40, (d) S-10@40 and (e) S-20@40, prepared at different reaction conditions.

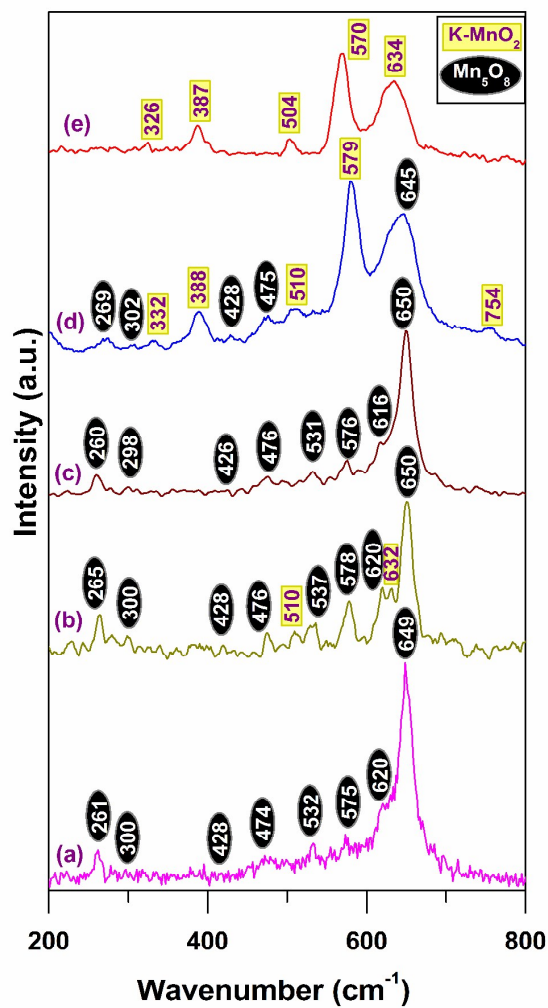


Figure 3: Raman spectra Mn oxides samples: (a) S-2@20, (b) S-2@80, (c) S-2@40, (d) S-10@40 and (e) S-20@40, prepared at different reaction conditions.

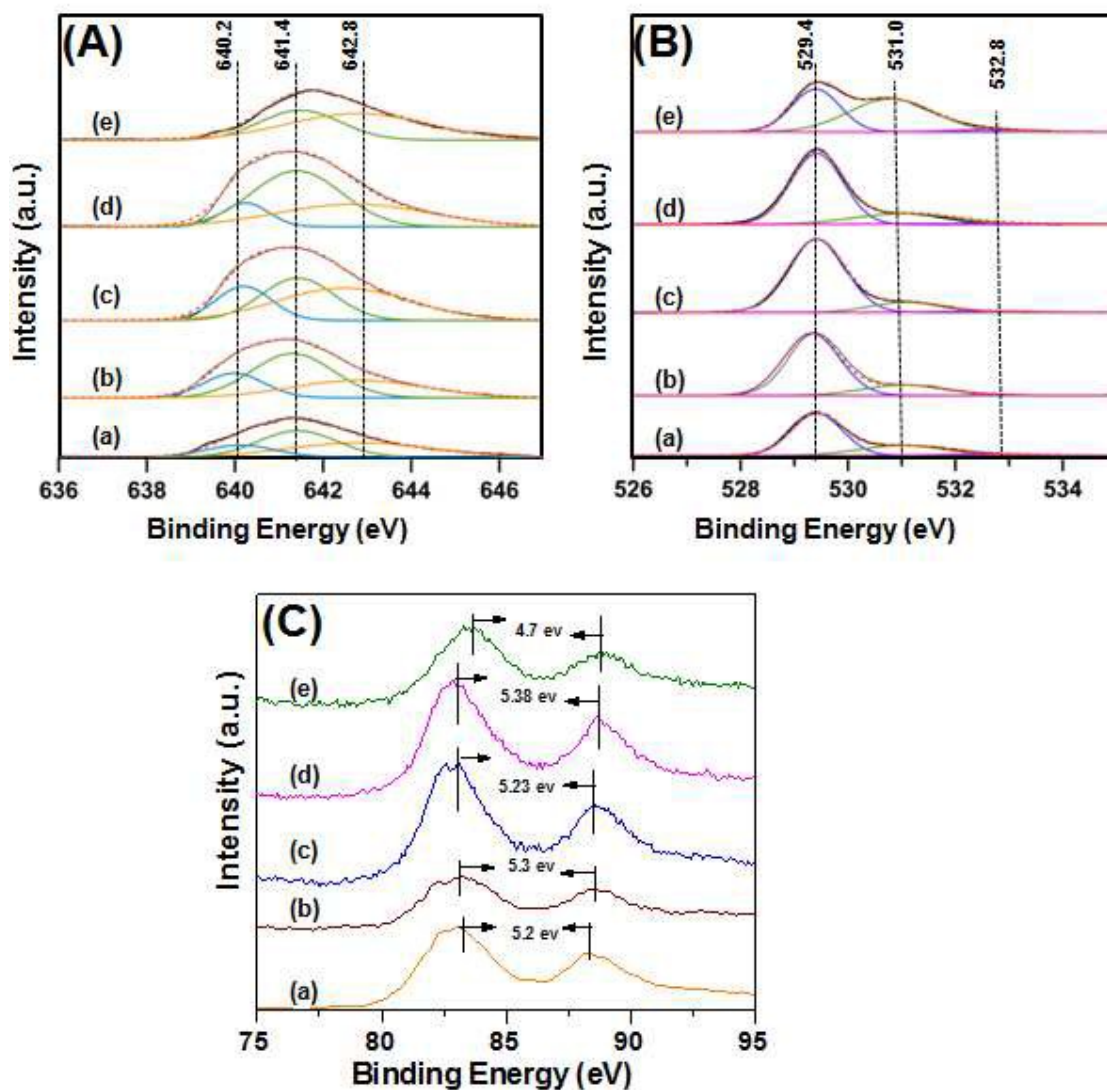


Figure 4: XPS spectra for (A) Mn 2p_{3/2}, (B) O 1s, and (C) Mn 3s of Mn oxide samples (a) S-2@20, (b) S-2@80, (c) S-2@40, (d) S-10@40 and (e) S-20@40, prepared at different reaction conditions.

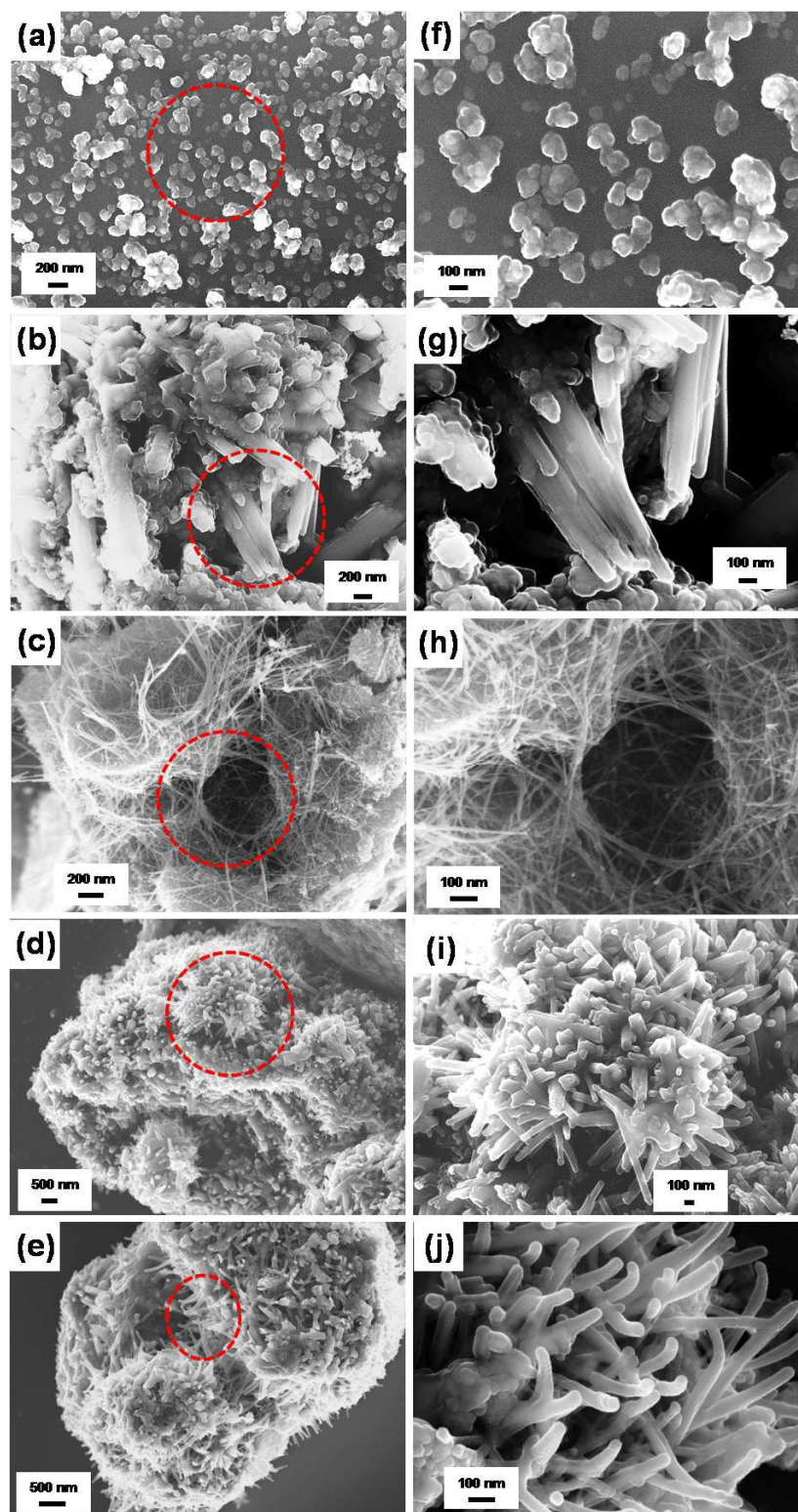


Figure 5: FESEM micrographs of Mn oxide samples (a) S-2@20, (b) S-2@80, (c) S-2@40, (d) S-10@40 and (e) S-20@40, (the corresponding higher magnified images are indicated in Figs. 5f-j)

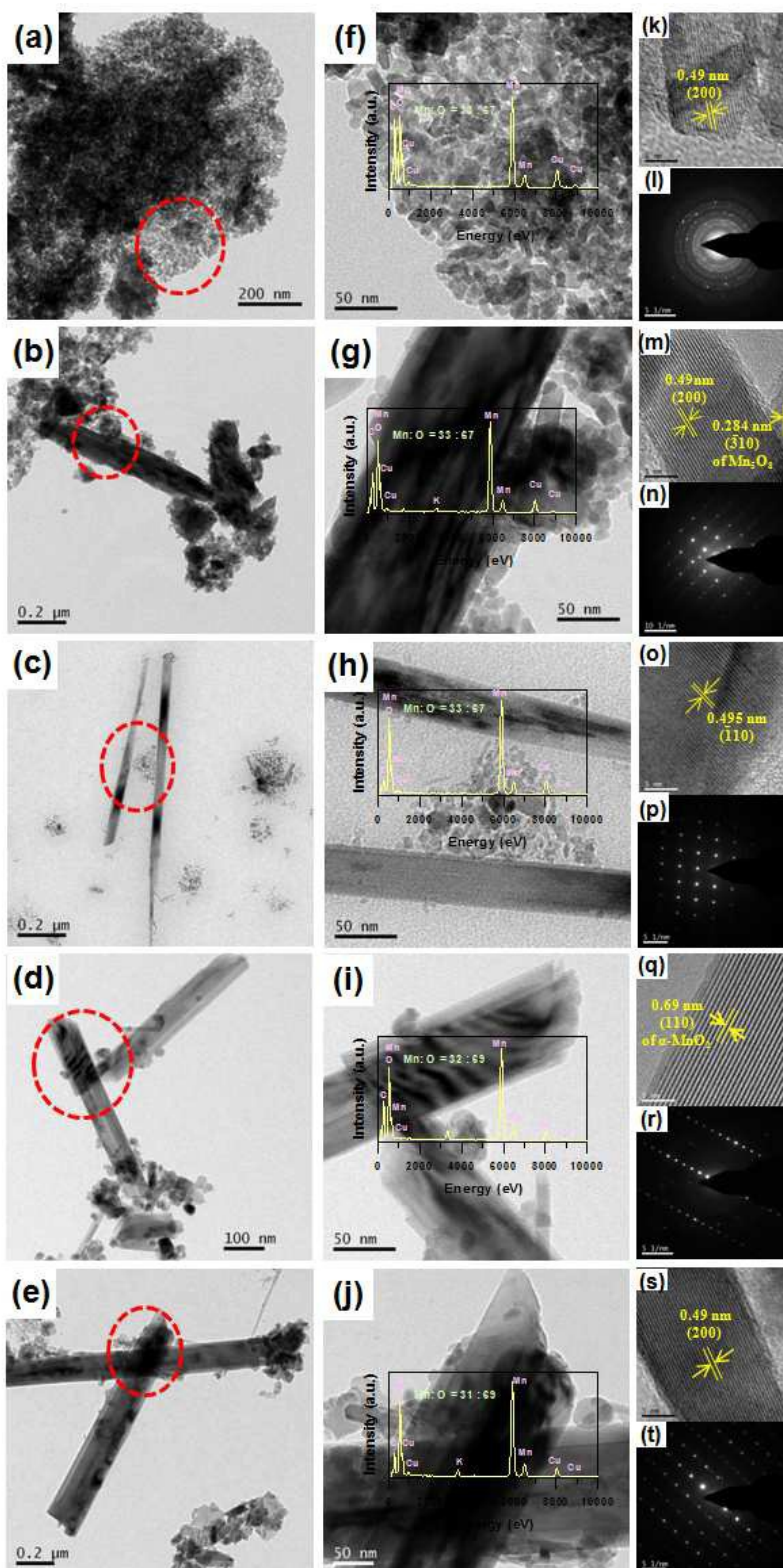


Figure 6: (a-e) TEM images, (f-j) magnified TEM images (with EDS at the inset), (k,m,o,q,s) HRTEM, (l,n,p,r,t) SAED pattern of Mn oxide samples S-2@20 (a,f,k,l), S-2@80 (b,g,m,n) S-2@40 (c,h,o,p), S-10@40 (d,i,q,r) and S-20@40 (e,j,s,t), respectively.

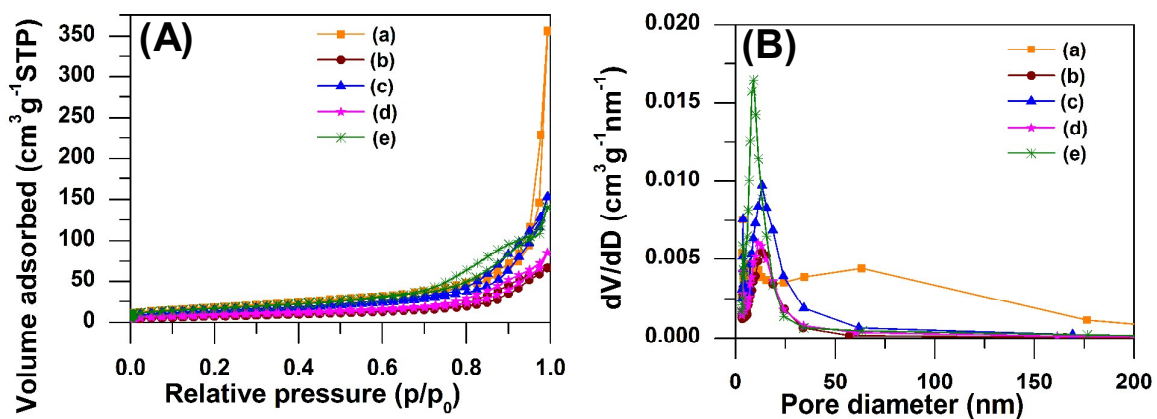


Figure 7: (A) N₂ adsorption-desorption isotherms and (B) Pore size distributions of Mn oxide samples (a) S-2@20, (b) S-2@80, (c) S-2@40, (d) S-10@40 and (e) S-20@40, prepared at different reaction conditions.

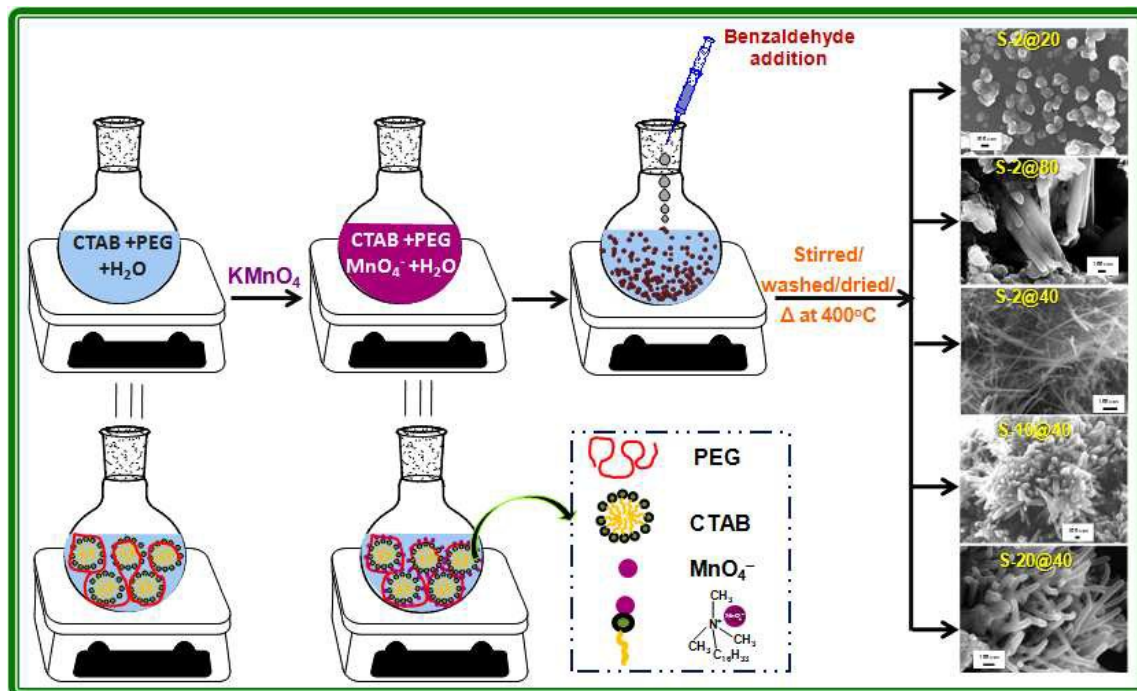


Figure 8: Schematics of the proposed formation mechanism of Mn oxides.

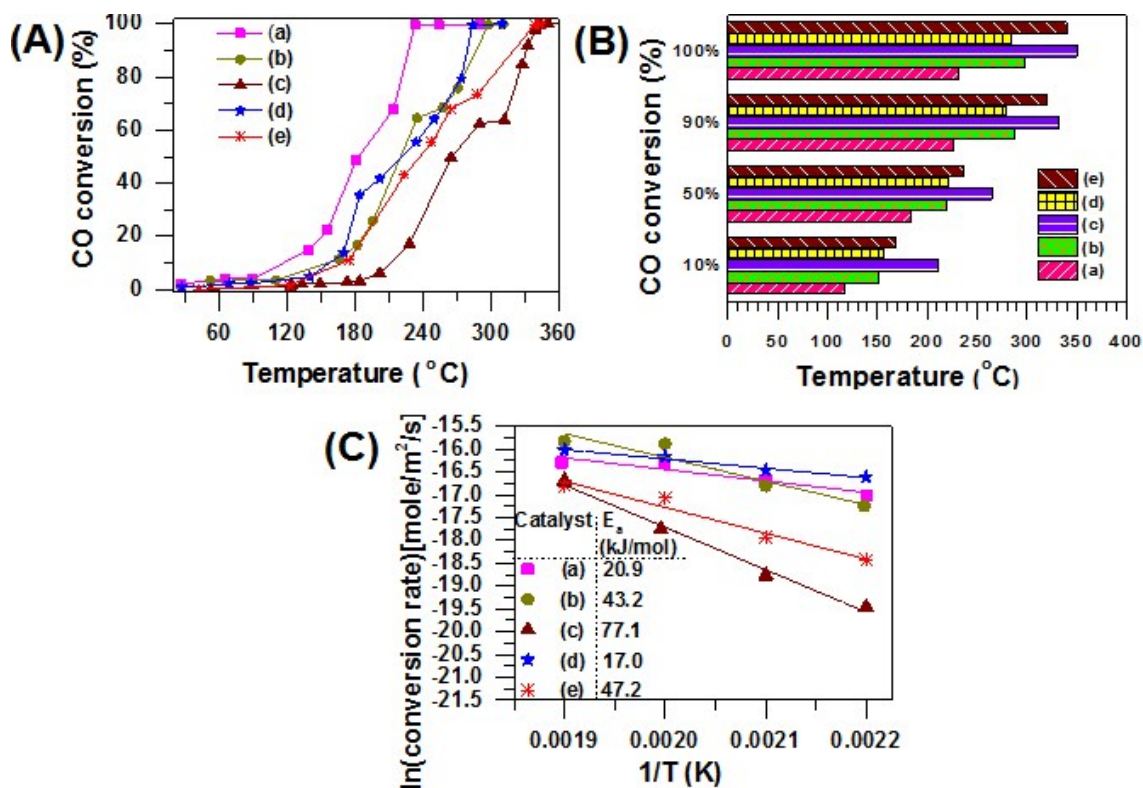


Figure 9: (A) Percentage of CO conversion as a function of temperature, (B) Temperatures corresponding to 10 % (T_{10}), 50% (T_{50}), 90% (T_{90}) and 100 % (T_{100}) CO conversion and (C) Arrhenius plot for CO oxidation with Mn oxide catalyst: (a) S-2@20, (b) S-2@80, (c) S-2@40, (d) S-10@40 and (e) S-20@40.

Table 1: Surface elemental compositions of the Mn oxide samples from Mn 2p_{3/2} and O1s XPS spectra.

Sample ID	Surface element molar ratio								
	Mn					O			
	Mn ²⁺	Mn ³⁺	Mn ⁴⁺	Mn ³⁺ / Mn ⁴⁺	Mn ³⁺ / Mn ²⁺	O _α	O _β	O (OH ⁻ / molecular water)	O _α / O _β
S-2@20	0.169	0.419	0.412	1.01	2.48	0.688	0.274	0.038	0.40
S-2@80	0.198	0.382	0.241	1.57	2.48	0.800	0.194	0.006	0.24
S-2@40	0.204	0.334	0.462	0.72	1.64	0.836	0.142	0.022	0.17
S-10@40	0.115	0.525	0.360	1.46	4.55	0.736	0.219	0.045	0.30
S-20@40	–	0.391	0.609	0.64	–	0.412	0.556	0.032	1.35

TOC Graphic

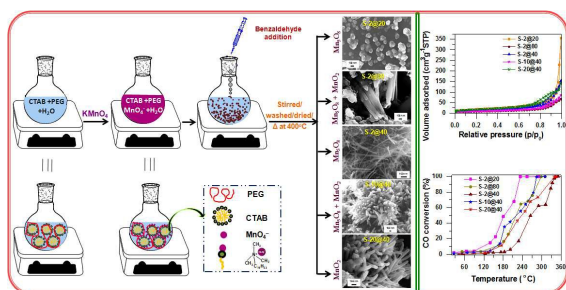
Bi-temple assisted synthesis of mesoporous manganese oxide nanostructures: Tailoring properties for efficient CO oxidation

Mouni Roy, Somjyoti Basak, and Milan Kanti Naskar*

Sol-Gel Division, CSIR-Central Glass and Ceramic Research Institute, Kolkata 700 032,

India

Bi-temple assisted synthesis of mesoporous manganese oxide catalysts with tuned morphology, crystal structure, textural property for efficient CO oxidation.



Electronic Supporting Information

Bi-template assisted synthesis of mesoporous manganese oxide nanostructures: Tailoring properties for efficient CO oxidation

Mouni Roy, Somjyoti Basak, and Milan Kanti Naskar*

Sol-Gel Division, CSIR-Central Glass and Ceramic Research Institute, Kolkata 700 032,

India

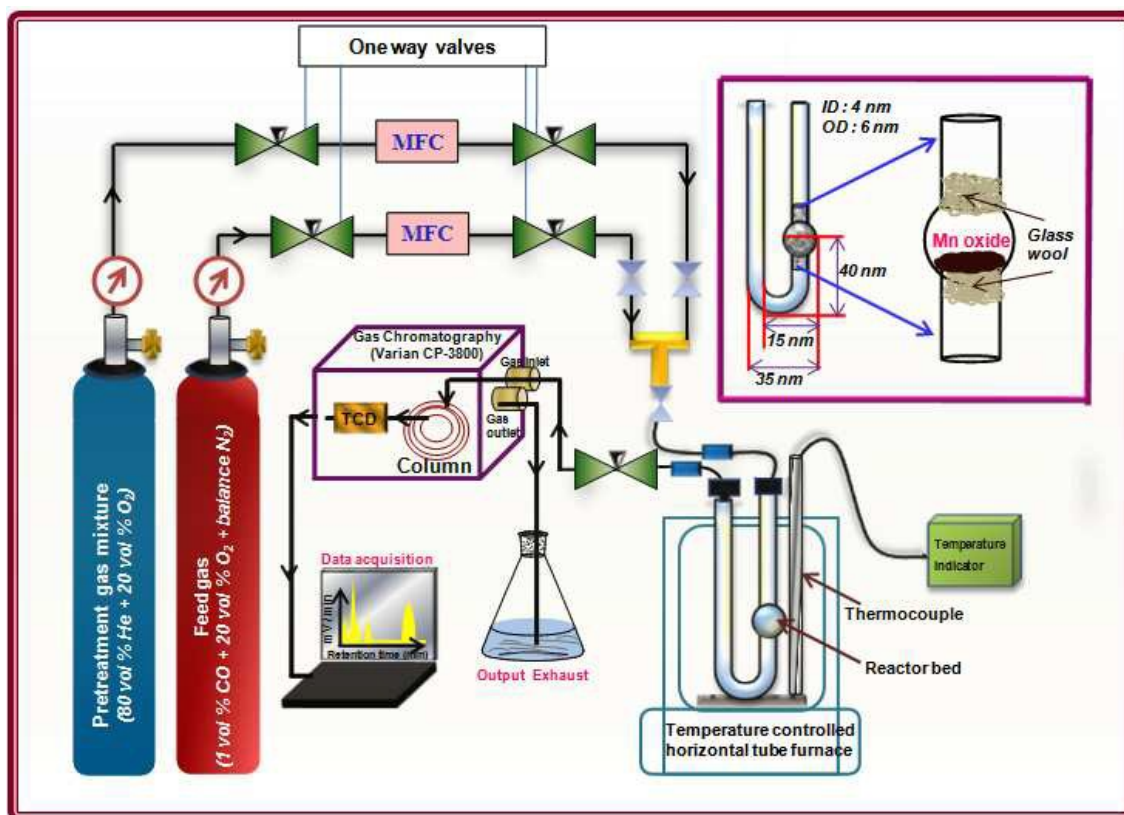


Figure S1: Schematic diagram of the experimental set-up for oxidative conversion of carbon monoxide.

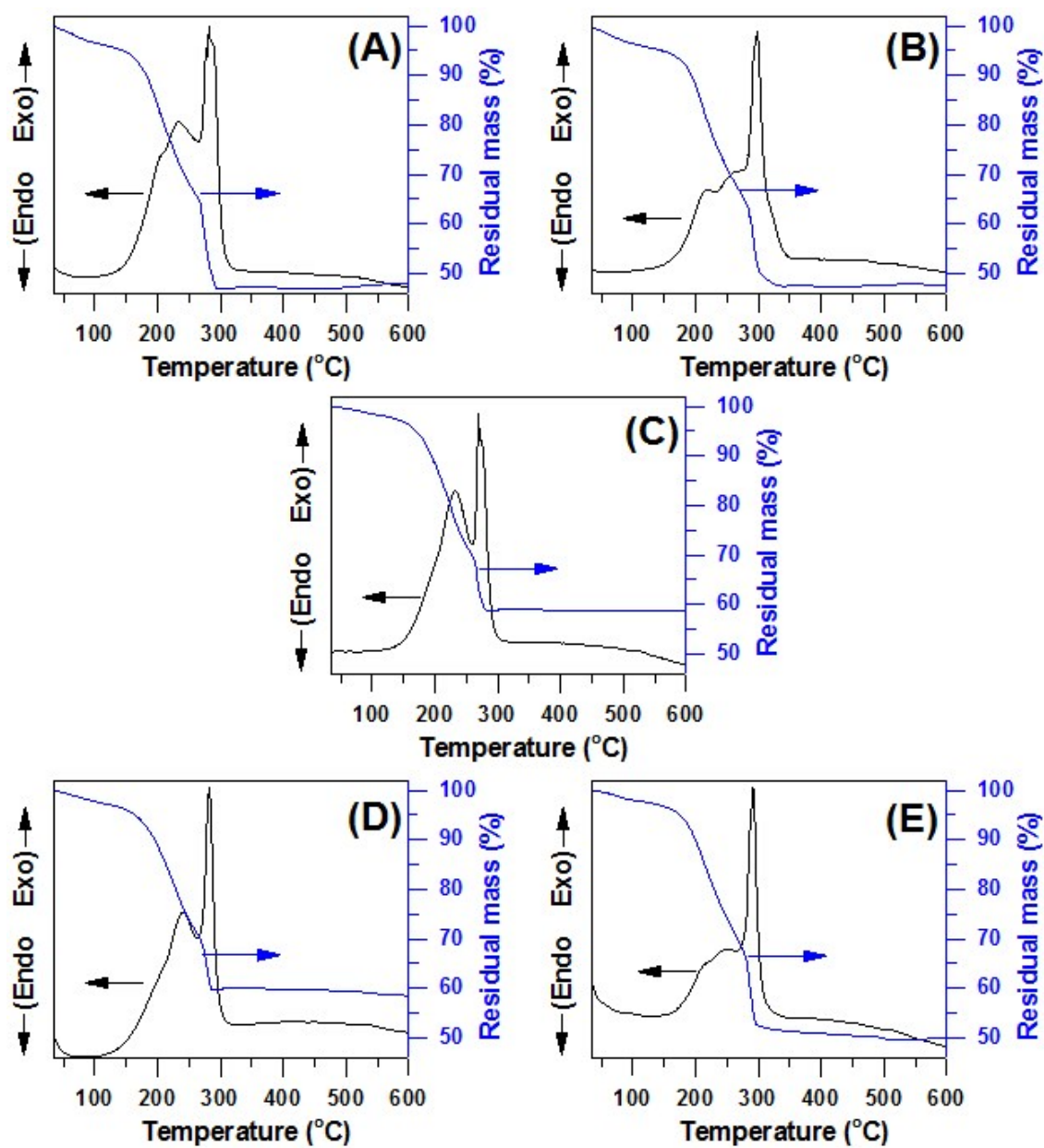


Figure S2: DTA-TG of Mn oxide samples before thermal treatment: (A) S-2@20, (B) S-2@80, (C) S-2@40, (D) S-10@40 and (E) S-20@40.

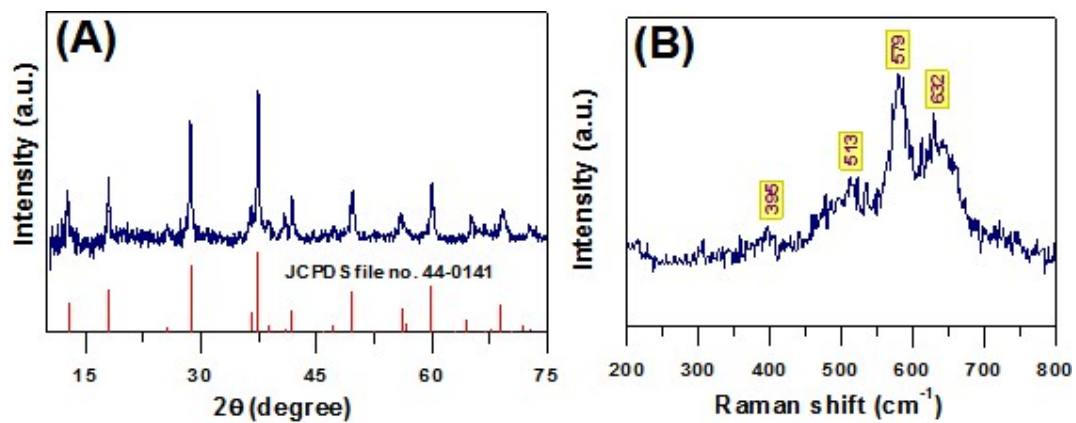


Figure S3: (A) XRD and (B) Raman spectra of Mn oxide prepared without benzaldehyde (S-2@0).

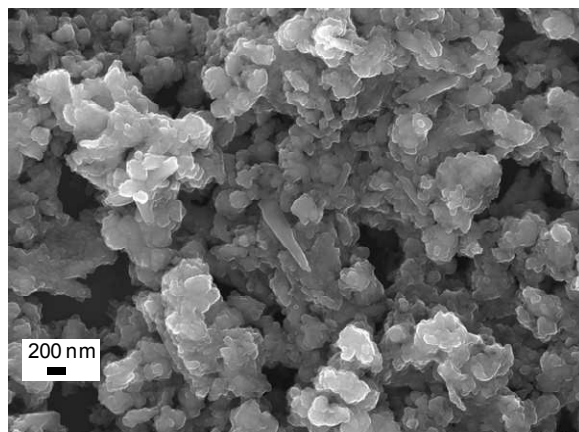


Fig. S4: FESEM image of Mn oxide prepared without benzaldehyde (S-2@0).

Table S1: The phase identified by XRD and Raman spectroscopy, and AOS determined by XPS analysis of different Mn oxides.

Sample ID	Phase identified by XRD and Raman spectroscopy	ΔE_s	Average oxidation state (AOS) ^a of Mn in oxides samples
S-2@20	Mn ₅ O ₈	5.20	3.1
S-2@80	Mn ₅ O ₈ + MnO ₂	5.30	3.0
S-2@40	Mn ₅ O ₈	5.23	3.1
S-10@40	Mn ₅ O ₈ + MnO ₂	5.38	2.9
S-20@40	MnO ₂	4.70	3.7

^a AOS = 8.956 - 1.126 ΔE_s , where ΔE_s = binding energy obtained from doublet separation of Mn3s

Table S2: The textural property of prepared Mn oxide samples

Sample ID	S _{BET} (m ² g ⁻¹)	V _{p-Total} (cm ³ g ⁻¹)	D ^a (nm)
S-2@20	65	0.55	34.2
S-2@80	28	0.10	15.5
S-2@40	48	0.24	19.8
S-10@40	32	0.13	16.6
S-20@40	61	0.22	14.2

^a Average pore diameter

Table S3: The temperatures corresponding to CO oxidations with the prepared Mn oxide catalysts

Catalyst ID	Temperature for CO conversion			
	T _{10%}	T _{50%}	T _{90%}	T _{100%}
S-2@20	117	183	227	232
S-2@80	152	220	287	298
S-2@40	211	265	332	350
S-10@40	157	221	279	284
S-20@40	168	237	320	340

Table S4: Data of research papers regarding activation energy required for CO oxidation over Mn oxide catalysts

Type of oxide	Conditions	T _z °C	E _a (kJ/mol)	Ref. no.
Mn ₂ O ₃	1% CO, 18% O ₂ ; GHSV=10,000 h ⁻¹	T ₅₀ = 423	46.05	1
α-MnO ₂	1% CO, 16% O ₂ ; D _{total} =100 mlmin ⁻¹ ; m=150 mg	T ₉₀ = 399	–	2
δ-MnO ₂	5% CO, 21% O ₂ ; D _{total} =21 mL min ⁻¹ ; m = 1 g	T ₄₅ = 353	20.93	3
3DOM Mn ₂ O ₃	1% CO, 20% O ₂ ; GHSV=20,000 h ⁻¹ ; m=500 mg	T ₉₀ = 180	80	4
α-Mn ₂ O ₃	1% CO, 20% O ₂ ; D _{total} = 50 mL min ⁻¹ ; m = 50 mg	T ₅₀ = 407	37	5
MnO _x	2% CO, 2% O ₂ ; D _{total} = 50 mlmin ⁻¹ ; m=20 mg	T ₉₀ = 410	17	6
Non-stoichiometric Mix phase (Mn ₅ O ₈ +MnO ₂)	1% CO, 20% O ₂ ; D _{total} = 40 mlmin ⁻¹ ; m=50 mg	T ₉₀ = 279	17	Present work

References:

1. S. Imamura, H. Sawada, K. Uemura and S. Ishida, *J. Catal.*, 1988, **109**, 198-205.
2. R. Xu, X. Wang, D. Wang, K. Zhou and Y. Li, *J. Catal.*, 2006, **237**, 426-430.
3. S. B. Kanungo, *J. Catal.*, 1979, **58**, 419-435.
4. S. Xie, H. Dai, J. Deng, H. Yang, W. Han, H. Arandiyani and G. Guo, *J. Hazard. Mater.*, 2014, **279**, 392-401.
5. L.-C. Wang, X.-S. Huang, Q. Liu, Y.-M. Liu, Y. Cao, H.-Y. He, K.-N. Fan and J.-H. Zhuang, *J. Catal.*, 2008, **259**, 66-74.
6. V. Iablokov, K. Frey, O. Geszti and N. Kruse, *Catal. Lett.*, 2010, **134**, 210-216.